



Enhanced photon-to-electron conversion and improved water resistance of hydrogenated ceria in photocatalytic oxidation at gas–solid interface



Dong Jiang^{a,b}, Wenzhong Wang^{a,*}, Yali Zheng^{a,b}, Ling Zhang^a

^a State Key Laboratory of High Performance Ceramics and Superfine Microstructure, Shanghai Institute of Ceramics, Chinese Academy of Sciences, 1295 Dingxi Road, Shanghai 200050, PR China

^b University of Chinese Academy of Sciences, Beijing 100049, PR China

ARTICLE INFO

Article history:

Received 6 February 2016

Received in revised form 11 March 2016

Accepted 12 March 2016

Available online 14 March 2016

Keywords:

Defect engineering

Photocatalysis

Oxygen vacancies

Water resistance

Gas–solid interface

ABSTRACT

Hydrogenation has been widely employed in solar-driven photocatalysis, to enhance the light absorption and photon-to-electron (PE) conversion of semiconductors. However, there still remain controversies in this field, such as the precise roles of bulk and surface oxygen vacancies (V_O). Furthermore, the influence of hydrogenation on surface reactions in photocatalysis at gas–solid interface has been rarely discussed. Herein, gray CeO_2 was prepared by treating pristine CeO_2 in H_2/Ar , presenting surface plasma resonance (SPR) like visible light absorption. No modifications on microstructural surface disordering or valence band edge were detected in gray CeO_2 . Hydrogenation induced abundant V_O inside both the bulk lattice and the surface layer. Gray CeO_2 presented much enhanced performance as well as improved water resistance in photocatalytic oxidation of gaseous hydrocarbons. Additional post-annealing in air was applied to remove surface V_O and discolored the material. With series of characterization including XPS, Raman, EPR and in-situ FTIR, it was found bulk V_O mostly contributes to the enhanced PE conversion, while surface V_O is mainly responsible for the improved water resistance. Our results unambiguously confirmed hydrogenation as an efficient approach to simultaneously optimize oxide semiconductors in various elementary steps of photocatalysis.

© 2016 Elsevier B.V. All rights reserved.

1. Introduction

Solar-driven semiconductor photocatalysis has attracted world-wide attention for its promising potentials in energy and environmental uses [1,2]. Defect engineering (DE) is one commonly employed approach to tailor both the electronic and optical properties of various materials [3–6]. Especially since the black TiO_2 reported by Chen et al. in 2011, hydrogenation and analogous reductive treatment have initiated a flourishing interest in this field to promote solar energy conversion [7–13]. For hydrogenated materials, the enhanced photoreactivity has been widely attributed to broadening light absorption and improved charge separation. However, insights into the efficacy of hydrogenation are multifarious and progressive over the past few years. Controversies have been general on the physical and chemical properties of modified materials, including the origin of visible-light absorption [8,13,14],

the existence of surface structural disorder [13–16], the modifications of valence band edge [8,14,17,18], the spatial distribution of surface and bulk defects [10–12,19], and even the superiority of hydrogenation itself [3,20]. For example, the white TiO_2 can turn into yellow, gray, black or blue after H_2 treatment, and such color changes have been attributed to microstructural surface disorder, mid-gap levels from structural nonstoichiometry or induced rearrangement of surface defects [8,11–15,18–22]. The inconsistencies probably come from the very different nature of materials applied as well as conditions for hydrogenation. These complexities, on the other hand, provide us with potential opportunities to explore novel structure-function relationship towards various applications.

Heterogeneous photocatalysis is the integration of photo-excitation and surface catalysis. Photo-excitation involves light absorption and charge carriers output, while surface catalysis concerns the utilization of photogenerated e^-/h^+ pairs [1,23,24]. For ideal solar energy utilization, synergy among various elementary steps is required. Most present DE studies focus on the modifications of photo-excitation. In addition to the broadening of light absorption, the improved charge transport and

* Corresponding author.

E-mail address: wzwang@mail.sic.ac.cn (W. Wang).

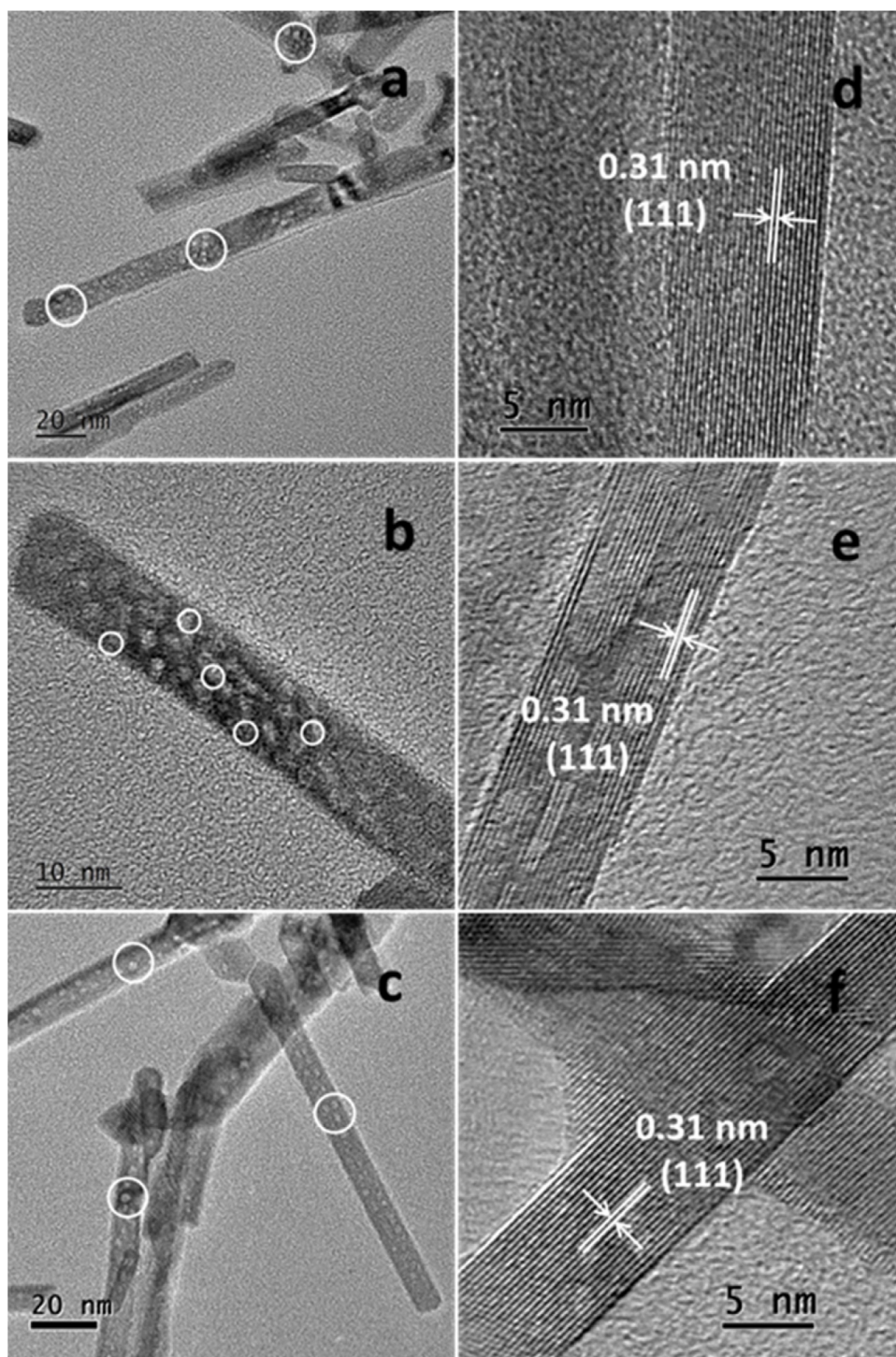


Fig. 1. Transmission electron microscopy (TEM) images of A-CeO₂ (a), H-CeO₂ (b) and A-H-CeO₂ (c). High-resolution TEM (HRTEM) images of A-CeO₂ (d), H-CeO₂ (e) and A-H-CeO₂ (f).

separation are proposed to stem from the induced oxygen vacancies (V_O) during hydrogenation, which serve as electron donors [15,18,21,22,25–27]. As for the roles of V_O , different views have been proposed. Some results indicated only surface V_O contributes to charge separation [10,20,28,29], while some results proved bulk V_O did benefit charge transport inside the lattice [15,18,19]. For the present, influence of hydrogenation on surface catalysis step, on the other hand, has been less discussed [30]. For heterogeneous catalysis, surface reactants (e.g. oxygen, dyes, etc.) activation at the gas/liquid-solid interfaces is of vital importance

[23,24,30–32]. However, in photo-oxidation of gaseous organics, we usually neglect the competitive adsorption of H₂O, which has been widely reported to be poisonous in various processes, such as CO oxidation, selective catalytic reduction (SCR), and so on [33–35]. In this respect, given the modified surface nature (i.e. surface defects) of hydrogenated solids, regulation of surface catalysis in solar-driven photocatalysis can be expected.

Fluorite CeO₂ with mixed electronic and ionic conduction has been versatile in various applications. The relatively positive valence band (VB) position makes CeO₂ a suitable candidate

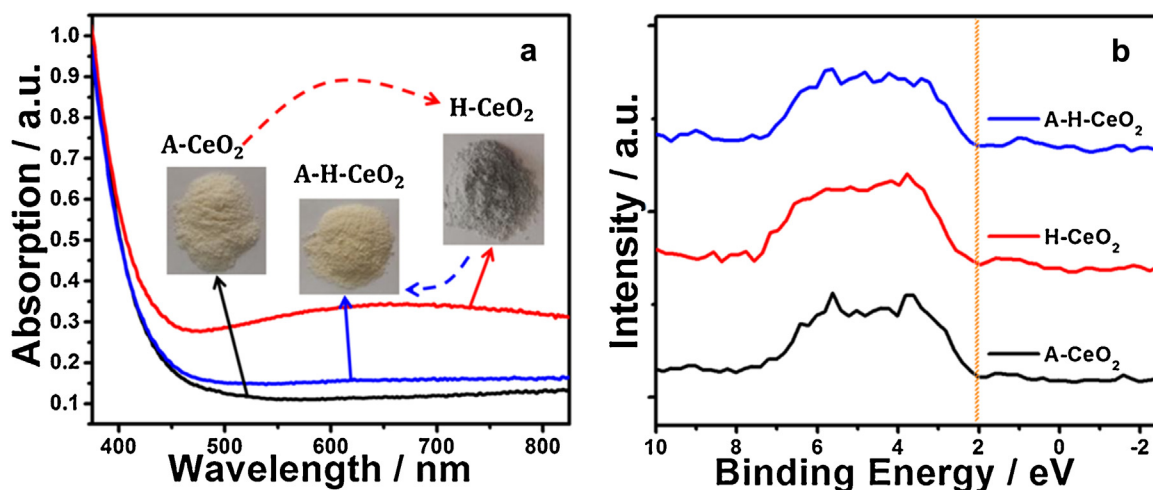


Fig. 2. UV-vis diffuse reflectance spectra (DRS) (a) and valence band X-ray photoelectron spectroscopy (VB-XPS) (b) of A-CeO₂, H-CeO₂ and A-H-CeO₂. Insets in the left panel are the digital photographs of annealed samples.

for photocatalytic oxidation [23,36–38]. Due to the repeatable Ce⁴⁺/Ce³⁺ cycles on the surface, CeO₂ has been employed as an active component or catalyst support [39–41]. Therefore, CeO₂ can provide us a perfect platform for exploring the synergy between photo-excitation and surface catalysis via defect engineering. In this work, gray CeO₂ was prepared by treating the pristine CeO₂ in a H₂/Ar flow. H₂ treatment induced abundant oxygen vacancies inside both the bulk lattice and the surface layer. The greatly increased donor density enhanced the transport and separation of charge carriers, and induced a surface plasma resonance (SPR) like absorption in the range of 400–900 nm. Hydrogenation brought about no modifications on both the microstructural surface disordering and the valence band edge of annealed CeO₂. Gray CeO₂ presented much enhanced performance and water resistance in photocatalytic oxidation of gaseous hydrocarbons (HC). In order to explore the precise roles of bulk and surface V_O, post-annealing in air was further applied to remove the surface V_O and discolored the material. Based on scientific studies, it was concluded that bulk V_O mostly contributes to the enhanced photon-to-electron conversion, while surface V_O is mainly responsible for the improved water resistance.

2. Experimental

2.1. Material preparation

Ce(NO₃)₃·6H₂O (99.5% purity) was obtained from Aladdin Reagents, Shanghai. NaOH of analytical purity was obtained from Sinopharm Reagent Co. Ltd., CeO₂ nanorods were prepared via a reported hydrothermal method. Briefly, 2.5 g of Ce(NO₃)₃·6H₂O were dissolved in 10 mL deionized water and the solution was quickly injected into another NaOH aqueous solution (8 M, 30 mL). After stirring for 15 min, the formed suspension was transferred to a 50 mL Teflon lined stainless steel autoclave, and then heated at 110 °C for 24 h. Afterwards, the precipitates obtained were washed with deionized water, followed by drying at 60 °C overnight and calcination at 400 °C for 3 h in air, successively. H-CeO₂ was prepared by treating the pristine CeO₂ in a 10% H₂/Ar flow at 700 °C for 1 h, with a heating rate of 10 °C min⁻¹. A-H-CeO₂ was obtained by annealing H-CeO₂ in air (200 °C/1 h). For comparison, A-CeO₂ prepared by heating pristine CeO₂ in air (700 °C/1 h) was employed.

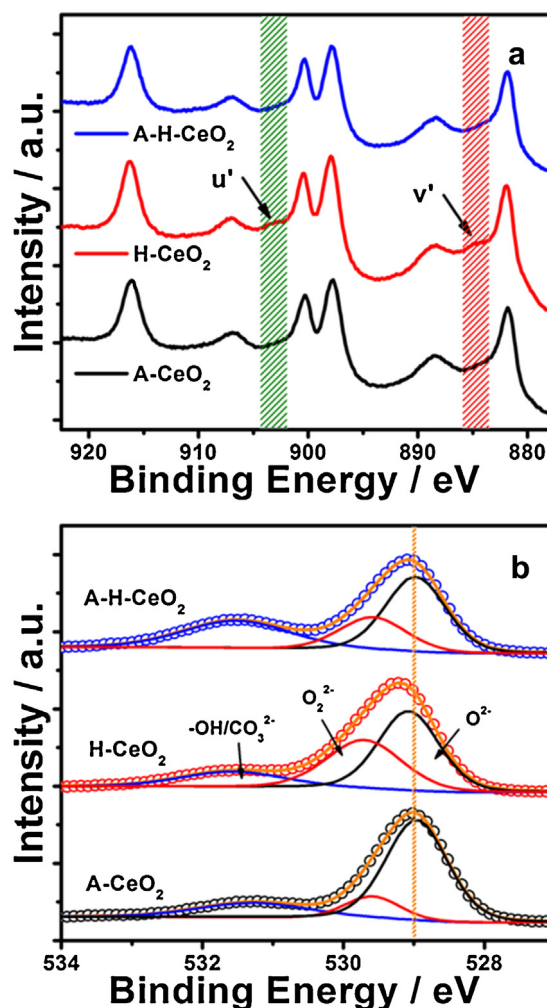


Fig. 3. X-ray photoelectron spectroscopy (XPS) of annealed A-CeO₂, H-CeO₂ and A-H-CeO₂ samples in Ce 3d (a) and O 1s (b) regions.

2.2. Characterization

The X-ray diffraction patterns were recorded on a Rigaku D/MAX 2250V diffractometer. The morphology and microstruc-

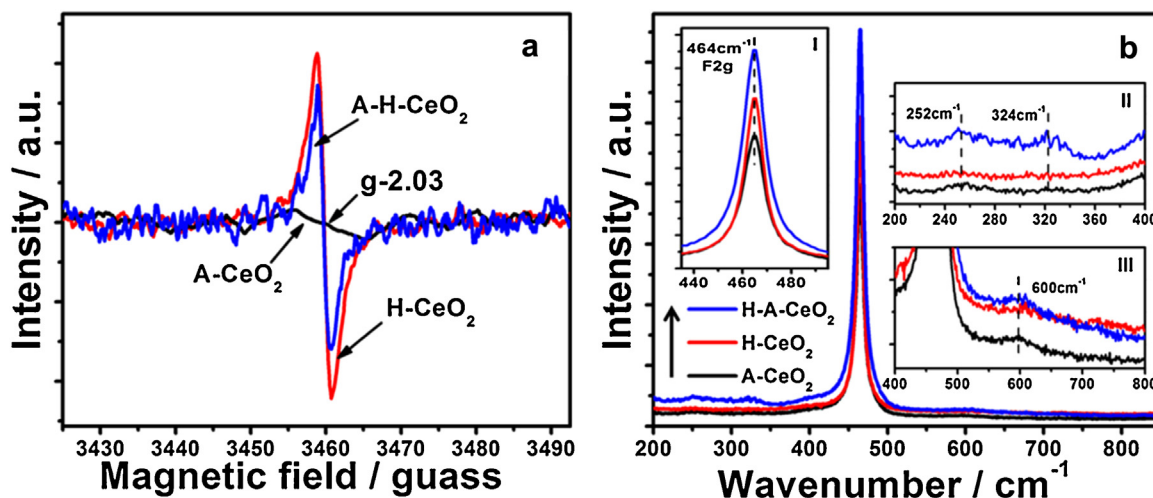


Fig. 4. Electron paramagnetic resonance (EPR) (a) and Raman spectra with 532 nm excitation (b) of annealed CeO_2 at room temperature. Insets are enlarged views of Raman data.

ture of annealed CeO_2 were investigated by transmission electron microscopy (TEM) on a JEOL JEM-2100F. The N_2 -sorption measurements were performed at 77 K using a Micromeritics Tristar 3000 analyzer. The specific surface areas were calculated with the Brunauer–Emmet–Teller (BET) methods. Pore volume and pore size distribution plots were obtained by Barrett–Joyner–Halenda (BJH) method using the cylindrical pore model. The diffuse reflectance spectra (DRS) were obtained on a UV–vis spectrophotometer (Hitachi U-3010) using BaSO_4 as the reference. X-Ray photoelectron spectroscopy (XPS) analysis was performed on ESCALAB 250Xi (Thermo Scientific Ltd.). The C1s was used to correct the charge effects. Raman spectra were recorded on a Horiba LABRAM HR, with 532 nm excitation laser line. The electron paramagnetic resonance (EPR) spectra were obtained on a JEOL JES-FA 200 EPR spectrometer at room temperature. The water contact angles were measured on

a KINO SL200B contact angle meter. FTIR spectra were recorded on a Thermo Nicolet iS10 spectrometer, equipped with a DRIFTS cell (Harric Scientific Inc.). High-purity N_2 was used throughout the IR tests. A background spectrum was collected using 64 scans at room temperature after pretreated in a N_2 stream. Before each data collection, the temperature of the sample cell was adjusted within 1 min and kept stable for 20 min.

2.3. Photocatalytic tests

Annealed CeO_2 (100 mg) were applied in photocatalytic oxidation of gas mixture (30–60 ppm) of propane (C_3H_8) and propene (C_3H_6) in a static mode using dry cylinder gas. The tests were operated in a gas-closed vitreous reactor (600 mL) with a quartz window and a double-walled jacket. A Xe lamp (500 mW cm^{-2}) was

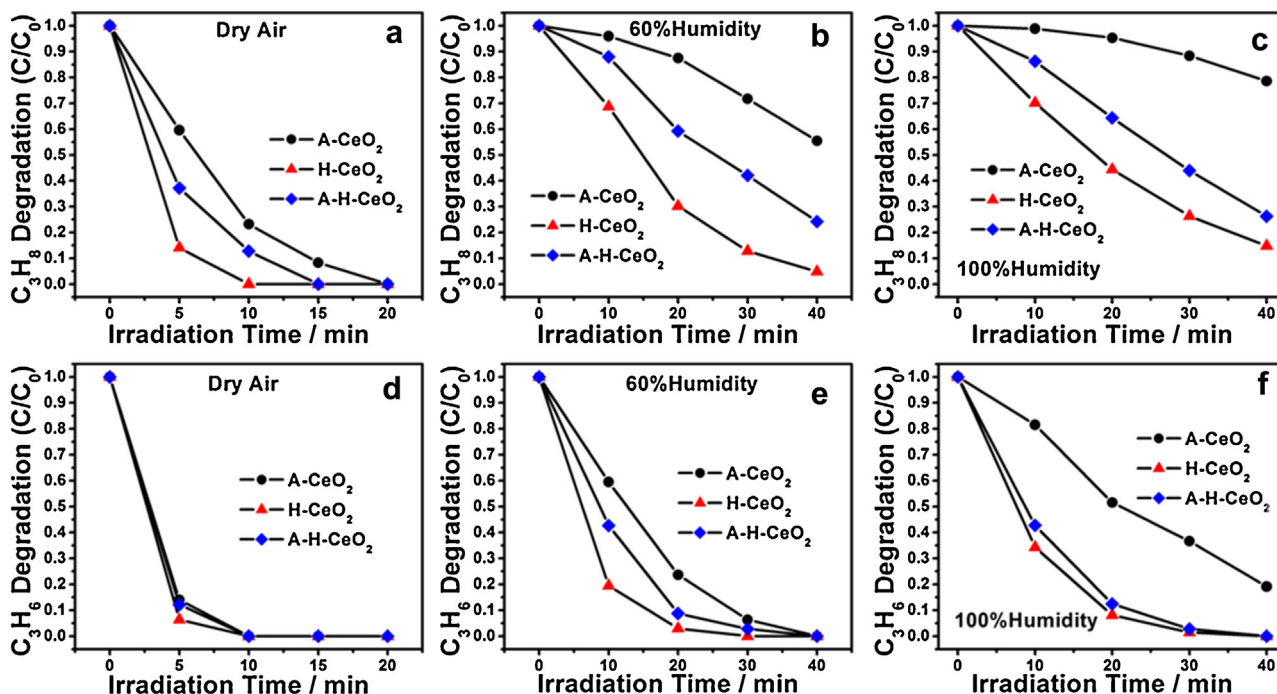


Fig. 5. Photocatalytic oxidation of the gas mixture of C_3H_8 (a–c) and C_3H_6 (d–f) over annealed CeO_2 under different conditions, dry air (a, d), 60% humidity (b, e) and 100% humidity (c, f).

used to simulate the sunlight irradiation. For visible light, a high-pass filter (>420 nm) was used. During hydrocarbon (HC) oxidation, the reaction temperature was kept at 25°C using the circulating water. Relative humidity (RH) was adjusted by injecting different amount of water into the reactor. The oxidation processes were monitored by HC decrease and CO_2 increase simultaneously by gas chromatographic (GC) analysis (GC 7900, Techcomp). The channel for HC detection consists of a TM plot- $\text{Al}_2\text{O}_3/\text{S}$ capillary column and a flame ionization detector (FID). The channel for CO_2 detection consists of a TDX-01, 80–100 mesh packed column followed by a methane conversion furnace and a FID.

2.4. Hydroxyl radicals ($\cdot\text{OH}$) generation

Photocatalytic OH formation under Xe lamp irradiation was monitored by photoluminescence (PL) using terephthalate acid (TPA) as a probe. Briefly, CeO_2 powders (30 mg) were added into deionized water (100 mL) containing NaOH (0.01 M) and TPA (3 mM). Prior to light irradiation, the suspension was stirred in the dark for 30 min. At given time intervals after irradiation, 3 mL of the suspension was centrifuged for fluorescence analysis using spectrophotometer (Hitachi F-4600). The formed 2-hydroxyterephthalic acid has a fluorescence signal around 425 nm with excitation of 315 nm light. The visible light was obtained using a high pass (>450 nm) filter.

2.5. Electrochemical analysis

The electrochemical analysis was performed on a CHI 660D electrochemical workstation (Chenhua) using a standard three electrode quartz cell. A Xe lamp (CHF-XM500) was used as the light source. To make a working electrode, CeO_2 powders were deposited on a 15×25 mm fluorine-doped tin oxide (FTO) substrate. Briefly, 10 mg of catalyst was suspended in 500 μL of ethanol. Then, 200 μL of above slurry was coated on the FTO glass. The current-time curves were collected at 0.4 V vs. SCE. A high-pass filter (>450 nm) was employed to obtain the visible light irradiation. Electrochemical impedance spectroscopy (EIS) was tested at the open circuit potential with the frequency from 1000 kHz to 0.1 Hz. The electrolyte was a 0.2 M Na_2SO_4 solution (pH 6.8) bubbled with nitrogen.

3. Results and discussion

Ceria (CeO_2) nanorods were prepared via a facile hydrothermal method, with the X-ray diffraction (XRD) patterns indexed to a cubic fluorite structure (Fig. S1 in SI). After annealing in various conditions, A- CeO_2 , H- CeO_2 and A-H- CeO_2 displayed identical diffraction patterns with pristine CeO_2 . The sharpening of diffraction peaks indicated the much improved crystallinity with grain growth, defect-healing, and strain release. Three annealed CeO_2 own similar BET surface areas of $57\text{--}63\text{ m}^2\text{ g}^{-1}$. The morphologies were studied by transmission electron microscopy (TEM). As shown in Fig. S2 in SI, annealed CeO_2 retained the rod-like morphology, except the damaged integrity of single nanorod and partial fusion between discrete nanorods. Interestingly, after annealing in air or H_2 at 700°C , there densely appeared bright spots throughout A- CeO_2 and H- CeO_2 , which were not found in pristine CeO_2 . Post-annealing in air at 200°C (A-H- CeO_2) did not recover the annealed samples.

In order to further explore the microstructures of annealed CeO_2 , TEM images with higher resolution were recorded. As circled in Fig. 1a–c, fine cavities with size of 2–4 nm randomly spread over the nanorod. These cavities did not change the single-crystalline nature of as-prepared nanorods (Fig. 1d–f). Recently, Seal et al. reported similar results and ascribed the cavities to agglomeration

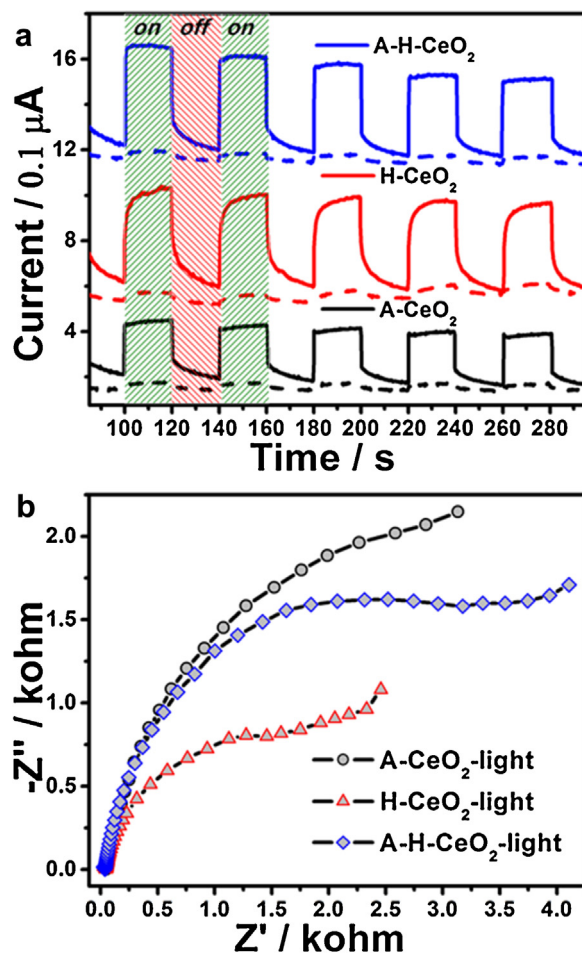


Fig. 6. Transient current-time (i-t) curves (a) under Xe lamp (solid line) and >450 nm light (dotted line) irradiation, and EIS Nyquist plots under Xe lamp irradiation (b) over three annealed CeO_2 electrodes.

of point defects during annealing [42]. These cavities are enclosed inside the bulk, confirmed by the N_2 -sorption measurements (Fig. S3 in SI), and thus cannot contribute to heterogeneous catalysis on the surface. More importantly, as indicated by the HRTEM images (Fig. 1d–f), all annealed samples were characterized by clean and distinct surfaces with perfect lattice fringes. This is different from previous reports, most of which claimed the appearance of an amorphous shell outside the crystalline core [8,9,13,14,16].

The optical and electronic structures of annealed CeO_2 were studied by UV-vis DRS and VB-XPS. As shown in Fig. 2a, compared to the nearly white A- CeO_2 , H- CeO_2 turned gray after hydrogenation with enhanced light absorption in the range of 400–900 nm, similar to the SPR absorption of noble metals. Actually, the hydrogenated sample was once deep purple in inert atmosphere, and gradually changed into gray when exposed to air (Fig. S4 in SI). This phenomenon suggested the reoxidation of surface reduced states or some kind of oxygen-induced surface rearrangement [12,19]. The gray coloration can be retained with exposure to air or water over 6 months. Post-annealing in air at 200°C was applied to H- CeO_2 to get A-H- CeO_2 , discoloring the gray sample. According to the band gap calculations (Fig. S5 in SI), neither hydrogenation nor post-annealing in air changed the band gap of CeO_2 nanorods (3.15 eV).

The VB-XPS of annealed CeO_2 were collected to study the modifications of valence band edge. As indicated in Fig. 2b, three annealed CeO_2 presented identical VB edges, 2.05 eV below the Fermi level. There appeared no shift of VB edge nor band tail above the VB maximum, which stems from the surface defects (e.g. $\text{Ti}^{3+}/\text{V}_0$ for

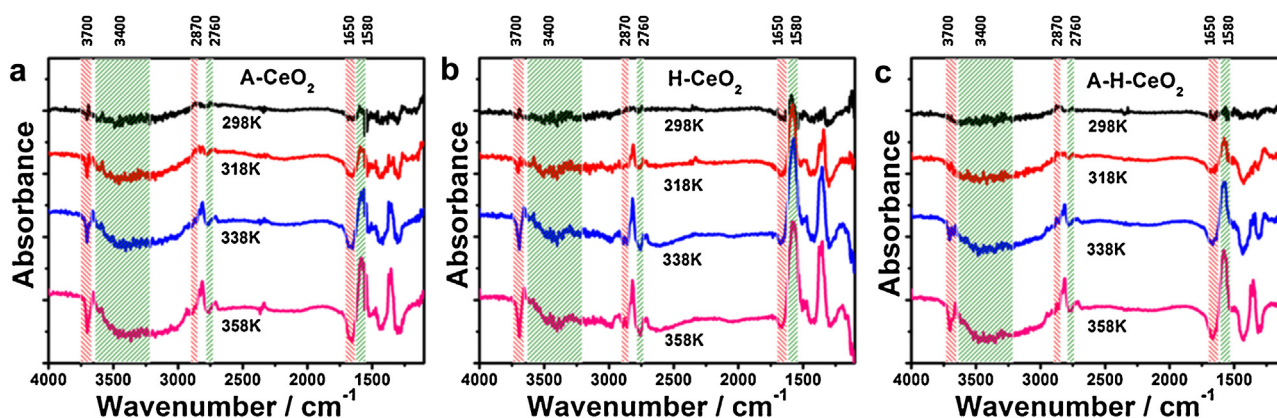


Fig. 7. TP-DRIFTS spectra of water desorption at elevated temperatures from the room temperature to 85 °C over A-CeO₂ (a), H-CeO₂ (b) and A-H-CeO₂ (c). The numerical ranges of absorbance in each vertical axis and relative position of each spectrum at specific temperatures are set to be the same.

TiO_{2-x}) [13,14]. Furthermore, VB-XPS were recorded after in situ Ar ion irradiation, effective to create a high Ce³⁺ concentration on CeO₂ surface [43–45]. In Fig. S6 in SI, additional electronic states within the band gap were accompanied with the production of abundant surface Ce³⁺ ions. This result, from another perspective, indirectly verified that hydrogenation didn't modify the electronic band structure. In this respect, the SPR-like absorption of H-CeO₂ can be attributed to collective excitations of greatly increased surface carriers (electrons) during hydrogenation, which were mostly quenched in by annealing in air.

In order to verify above speculation, the crystal defects within annealed CeO₂ were studied. After hydrogenation at 700 °C, both surface and bulk oxygen vacancies (V_O) can be induced in CeO₂ as supported by the temperature-programmed study (Fig. S7 in SI) [24,34]. Defects on the surface were characterized by X-ray photoelectron spectroscopy (XPS). As shown in Fig. 3a, the Ce 3d spectra display the coexistence of typical 3d_{3/2} and 3d_{5/2} spin-orbit components. The superposition of up to ten characteristic peaks makes it difficult to decide the precise content of Ce³⁺/Ce⁴⁺ ions. However, two Ce³⁺ (u' and v') peaks can be easily revealed in H-CeO₂, which in contrast is negligible in A-CeO₂ and A-H-CeO₂. That is, hydrogenation induced detectable Ce³⁺ on the surface, increasing the electrons density and inducing SPR-like absorption. Post-annealing in air mostly healed the surface defects and thus discolored the sample. Due to the charge conservation, presence of oxygen vacancies should accompany with surface Ce³⁺ ions. O 1s spectra of annealed CeO₂ (Fig. 3b) can be divided into three subpeaks, coming from the coexisted surface oxygen species [24,46,47]. The relative amount of lattice oxygen (O²⁻) on A-CeO₂ surface (68%) is much higher than that for H-CeO₂ (47%), indicating weaker surface integrity after hydrogenation. Besides, compared to A-CeO₂ (13.7%) and A-H-CeO₂ (22.7%), H-CeO₂ owns more O₂²⁻ species (36.3%). Increased chemisorbed O species on hydrogenated surface should be favorable for catalytic organics oxidation.

Defects in the bulk were probed using electron paramagnetic resonance (EPR) and Raman spectra. EPR is highly sensitive to unpaired electrons, such as Ti³⁺/V_O in TiO_{2-x} [8,9,48]. As shown in Fig. 4a, compared to the almost quiet signal of A-CeO₂, H-CeO₂ presented strong response at the g-value of 2.03, indicating the presence of abundant V_O [27,49,50]. After post-annealing in air, A-H-CeO₂ still retained most of the EPR signal, suggesting discoloration only eliminated surface V_O and barely influenced the bulk V_O. Additional evidence of the retention of bulk V_O in A-H-CeO₂ can be obtained from the Raman data (Fig. 4b). For A-H-CeO₂, both the broadening F_{2g} band centered at 464 cm⁻¹ and the enhanced peak intensity around 252 and 324 cm⁻¹ indicated the presence of abundant lattice defects in CeO₂ [32,49]. It is unexpected that

H-CeO₂ presented similar spectrum with A-CeO₂ and failed to give clear evidence of increased crystal defects. This phenomenon probably stemmed from the enhanced absorption of the excitation and scattering light (514 nm) by the hydrogenated sample [49,51]. That is, the Raman data here reflected more surface information rather than the bulk of H-CeO₂.

Hydrocarbons (HC) emitted from automobile exhaust are among the main sources of atmospheric pollutants [52–54]. Herein, annealed CeO₂ were applied for photooxidation of a gas mixture of propane (C₃H₈) and propene (C₃H₆) using Xe lamp as the light source. As shown in Fig. 5a and d, under simulated solar irradiation in dry air, C₃H₈ and C₃H₆ can be completely eliminated within 20 and 10 min, respectively. As monitored by GC analysis, neither propylene oxide (PO) nor other C1–C3 products but CO₂ was detected throughout the oxidation process, indicating the complete degradation of HC. Compared to A-CeO₂, gray H-CeO₂ presented much enhanced HC photooxidation, especially for C₃H₈ degradation. This difference probably stemmed from the enhanced C₃H₈ adsorption on the more defective H-CeO₂ surface. After post-annealing in air, discolored A-H-CeO₂ showed degraded performance, but was still superior to A-CeO₂. This reactivity order (i.e. H-CeO₂ > A-H-CeO₂ > A-CeO₂) evidently eliminated the exclusive role of surface defects or SPR-like photo-absorption in prompting the solar-driven HC oxidation. Above HC oxidation was conducted under visible light (>420 nm) irradiation (Fig. S8). All three CeO₂ samples presented similar photoreactivity, much weaker than that under Xe lamp irradiation, also suggesting that the gray coloration of hydrogenated CeO₂ was not the origin of its superiority in HC oxidation.

Furthermore, we studied the influence of moisture on HC oxidation. As shown in Fig. 5, with the increase of relative humidity (RH), all CeO₂ presented depressed performance. This trend should be attributed to the competitive adsorption between H₂O and HC as well as the low reactivity of –OH from H₂O dissociation on the surface [33,34]. Besides, the degradation of C₃H₈ was more greatly inhibited compared to that of C₃H₆, due to the weaker adsorption of less polar C₃H₈. Notably, compared to A-CeO₂, hydrogenated CeO₂ showed much improved water resistance, following the order of H-CeO₂ > A-H-CeO₂ > A-CeO₂. For example (Table 1), at 60% RH, the degradation ratios of C₃H₈ after 20 min and C₃H₆ after 10 min were 70 and 81% of that in dry air for H-CeO₂, but were only 13 and 41% for A-CeO₂. After post-annealing in air, A-H-CeO₂ presented moderate water resistance, retaining 41 and 57% performance for C₃H₈ and C₃H₆ removal.

From above results, it was concluded that hydrogenation can not only enhance the photocatalytic performance but also improve the water resistance in HC oxidation at solid-gas interface. Here-

Table 1
Degradation ratios (%) of C₃H₈ at 20 min and C₃H₆ at 10 min over annealed CeO₂ under different RH.

Samples & conditions	A-CeO ₂		H-CeO ₂		A-H-CeO ₂	
	C ₃ H ₈	C ₃ H ₆	C ₃ H ₈	C ₃ H ₆	C ₃ H ₈	C ₃ H ₆
Dry air	100	100	100	100	100	100
60% RH	13	41	70	81	41	57
100% RH	5	19	56	66	36	52

inafter, co-optimization of photo-excitation and surface catalysis steps will be in depth discussed. Firstly, the photon-to-electron (PE) conversion was investigated via electrochemical measurements. As shown in Fig. 6a, typical transient current responses via light on-off cycles were recorded over annealed CeO₂. Notably, H-CeO₂ and A-H-CeO₂ displayed much enhanced current responses upon light irradiation, about two times the amplitude of that over A-CeO₂. The difference, however, was not that obvious under the visible light irradiation. Given these results, it was the hydrogenation itself that enhanced the PE conversion, rather than the SPR-like light absorption. That is, the much enhanced PE conversion should be attributed to the increased electronic conduction stemming from the increased bulk donors in gray CeO₂ [15,18,19,22]. Electrochemical impedance spectra (EIS) were also recorded with three CeO₂ electrodes. As indicated in Fig. 6b, the arc radius of the Nyquist plot of H-CeO₂ was much smaller than that of A-CeO₂, indicating more effective separation of photo-induced e⁻/h⁺ pairs. After post-annealing in air, A-H-CeO₂ presented a mediate arc, the radius of which was between that of A-CeO₂ and H-CeO₂. Above electrochemical results suggested that for hydrogenated CeO₂, V_O inside the bulk mostly contributed to the improved charge separation in the photo-excitation step.

For surface catalysis step, attention was focused on the improved water resistance of hydrogenated CeO₂ during HC oxidation. On one hand, given the negative role of the competitive adsorption of H₂O, one conjecture was that CeO₂ turned less hydrophilic after H₂ treatment. However, as proved by the water contact angle tests (Fig. S9 in SI), H-CeO₂ was more hydrophilic than A-CeO₂ and A-H-CeO₂ with the smallest water contact angle of 17.8°. This is understandable because the increased electrons density from surface defects enhanced the surface polarity and thus promoted the dissociation of water [26,27,31,55–57]. On the other hand, increased hydroxyl (OH) groups from H₂O dissociation has been reported to favor the photo-induced adsorption of O₂ on a highly hydroxylated TiO₂ surface [58]. Fourier transform infrared (FTIR) spectra of annealed CeO₂ samples were recorded (Fig. S10 in SI), showing similar water-related absorption around 1650 and 3400 cm⁻¹ [59,60]. Based on above results, neither the hydrophilicity nor the amount of surface OH played the decisive role in deciding the water resistance.

In order to further explore the origin of difference in water resistance, in situ infrared spectra in diffuse reflectance mode (DRIFTS) were collected to study the temperature programmed (TP) water desorption from the surface of annealed CeO₂ [61–63]. In Fig. 7, the band centered at 1650 cm⁻¹ is attributed to the bending vibration of water (δ_{H2O}) and the broad band around 3400 cm⁻¹ is attributed to the symmetric and asymmetric stretching vibrations of hydroxyl groups (ν_{OH}) [59,60]. Besides, the negative feature at 3700 cm⁻¹ is attributed to the loss of isolated surface OH from the alkaline hydrothermal environment [60,64]. The decreased absorption at about 2870 and 2760 cm⁻¹ can be attributed to the removal of adventitious HC (δ_{C-H}) off the CeO₂ surface at elevated temperatures. The absorption centered at about 1357 and 1580 cm⁻¹ are characteristic of bicarbonate species stemmed from adsorbed CO₂ [65–67]. Similar report attributed the increased intensity of these bands to the protonation of carbonate by OH groups on the oxide

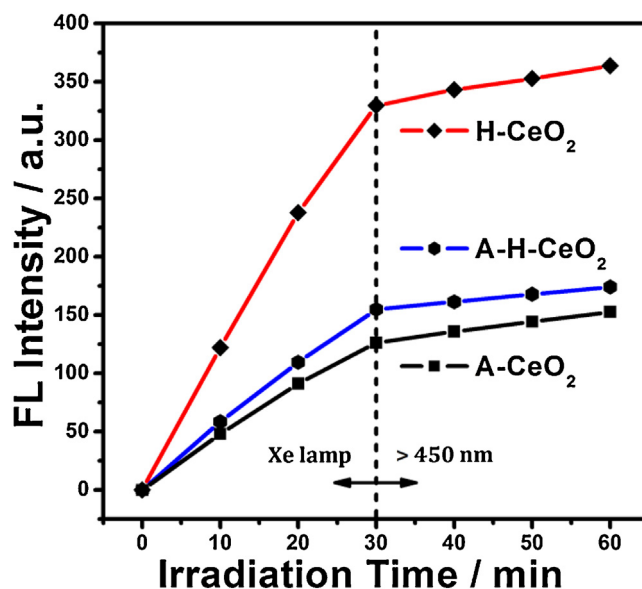


Fig. 8. Temporal evolution of fluorescence intensity at 425 nm with excitation of 315 nm light.

surface [67]. Compared to A-CeO₂ and A-H-CeO₂, H-CeO₂ presented the most intense increase of bicarbonate species on the surface. This difference probably came from the more defective nature of hydrogenated surface, which has been suggested to promote the activation of CO₂ due to higher electron-donating ability [5,65].

Notably, there existed obvious difference in the water desorption from the surface of three CeO₂. In Fig. 7, compared to that for A-CeO₂ and A-H-CeO₂, the decrease of water related absorption around 1650 and 3400 cm⁻¹ for H-CeO₂ was much slower. That is, the adsorbed H₂O from molecular adsorption or dissociation bonded more tightly to the hydrogenated surface. It has been suggested that surface OH can be photocatalytic transformed to •OH radicals with strong oxidative ability and favors the photocatalytic oxidation [34,59,68]. Based on the differences in water resistance and water desorption over three CeO₂, we propose one rational explanation. For photooxidation at gas-solid interface, only strongly bonded OH on the surface can be effectively utilized, while the weakly bonded OH or molecularly adsorbed H₂O just occupy and sacrifice the sites for reactants activation. In order to further verify this speculation, we tested photocatalytic •OH generation over three CeO₂ via a reported fluorescence method [24]. As shown in Fig. 8, H-CeO₂ presented the strongest fluorescence signal at 425 nm after 30 min Xe lamp irradiation, indicating its superiority in •OH generation. After switching to visible light (>450 nm), three CeO₂ presented slow •OH generation with no obvious difference. This phenomenon suggested that the SPR-like absorption was not the main reason for the outstanding photoreactivity of H-CeO₂ in •OH generation. Based on above discussion, the improved water resistance of hydrogenated H-CeO₂ is reasonable. Firstly, under solar irradiation, H-CeO₂ with gray coloration presents enhanced photothermic effect and partly expels the weakly adsorbed H₂O from the surface. Secondly, abundant V_O on H-CeO₂ surface promote the water dissociation and thus the subsequent generation of •OH radicals. Given that the gray coloration of H-CeO₂ also stems from the surface defects induced by hydrogenation, surface V_O should be mainly responsible for improved water resistance in HC oxidation.

4. Conclusion

In this work, gray CeO₂ was prepared by treating CeO₂ nanorods in a H₂/Ar flow. Neither discernible surface disorder layer nor modifications on the valence band edge were detected after hydrogenation. H₂ treatment induced abundant V_O inside both the bulk lattice and the surface layer. V_O on the surface induced a SPR-like absorption in the visible light range from 400 to 900 nm. Hydrogenated CeO₂ presented much enhanced performance as well as improved water resistance in photocatalytic oxidation of gaseous HC. In order to explore the precise roles of bulk and surface V_O, post-annealing in air was applied to remove surface V_O and discolored the gray CeO₂. It was found that bulk V_O mostly contributes to the enhanced photon-to-electron conversion, while surface V_O is mainly responsible for the improved water resistance. On one hand, bulk V_O served as electron donors and greatly promoted the transport of photogenerated charge carriers within CeO₂. On the other hand, surface V_O promoted the H₂O dissociation and weakened the negative role of competitive adsorption between H₂O and reactants, and thus brought about improved water resistance.

Acknowledgments

We acknowledge the financial support from the National Basic Research Program of China (2013CB933200) and the National Natural Science Foundation of China (51272269, 51272303, and 51472260).

Appendix A. Supplementary data

Supplementary Information (SI) available: XRD patterns, TEM images, N₂-sorption measurements, band gap estimation, XPS data after Ar ion irradiation, H₂-TPR profiles, water contact angles measurements and FTIR data of annealed CeO₂. Supplementary data associated with this article can be found, in the online version, at <http://dx.doi.org/10.1016/j.apcatb.2016.03.027>.

References

- [1] Y. Ma, X. Wang, Y. Jia, X. Chen, H. Han, C. Li, *Chem. Rev.* 114 (2014) 9987.
- [2] M.R. Hoffmann, S.T. Martin, W. Choi, D.W. Bahnemann, *Chem. Rev.* 95 (1995) 69.
- [3] L. Liu, X. Chen, *Chem. Rev.* 114 (2014) 9890.
- [4] J. Nowotny, M.A. Alim, T. Bak, M.A. Idris, M. Ionescu, K. Prince, M.Z. Sahdan, K. Sopian, M.A. Mat Teridi, W. Sigmund, *Chem. Soc. Rev.* 44 (2015) 8424.
- [5] D. Jiang, W. Wang, E. Gao, S. Sun, L. Zhang, *Chem. Commun.* 50 (2014) 2005.
- [6] Y. Lv, Y. Zhu, Y. Zhu, *J. Phys. Chem. C* 117 (2013) 18520.
- [7] X. Chen, L. Liu, F. Huang, *Chem. Soc. Rev.* 44 (2015) 1861.
- [8] Z. Wang, C. Yang, T. Lin, H. Yin, P. Chen, D. Wan, F. Xu, F. Huang, J. Lin, X. Xie, M. Jiang, *Adv. Funct. Mater.* 23 (2013) 5444.
- [9] C. Yang, Z. Wang, T. Lin, H. Yin, X. Lü, D. Wan, T. Xu, C. Zheng, J. Lin, F. Huang, X. Xie, M. Jiang, *J. Am. Chem. Soc.* 135 (2013) 17831.
- [10] Y. Lv, Y. Liu, Y. Zhu, Y. Zhu, *J. Mater. Chem. A* 2 (2014) 1174.
- [11] F. Zuo, L. Wang, T. Wu, Z. Zhang, D. Borchardt, P. Feng, *J. Am. Chem. Soc.* 132 (2010) 11856.
- [12] A. Naldoni, M. Allieta, S. Santangelo, M. Marelli, F. Fabbri, S. Cappelli, C.L. Bianchi, R. Psaro, V. Dal Santo, *J. Am. Chem. Soc.* 134 (2012) 7600.
- [13] X. Chen, L. Liu, Y.Y. Peter, S.S. Mao, *Science* 331 (2011) 746.
- [14] X. Chen, L. Liu, Z. Liu, M.A. Marcus, W.-C. Wang, N.A. Oyler, M.E. Grass, B. Mao, P.-A. Glans, P.Y. Yu, J. Guo, S.S. Mao, *Sci. Rep.* 3 (2013) 1510.
- [15] Z. Lu, C.-T. Yip, L. Wang, H. Huang, L. Zhou, *ChemPlusChem* 77 (2012) 991.
- [16] T. Xia, C. Zhang, N.A. Oyler, X. Chen, *Adv. Mater.* 25 (2013) 6905.
- [17] W. Wei, N. Yaru, L. Chunhua, X. Zhongzi, *RSC Adv.* 2 (2012) 8286.
- [18] G. Wang, H. Wang, Y. Ling, Y. Tang, X. Yang, R.C. Fitzmorris, C. Wang, J.Z. Zhang, Y. Li, *Nano Lett.* 11 (2011) 3026.
- [19] J. Qiu, S. Li, E. Gray, H. Liu, Q.-F. Gu, C. Sun, C. Lai, H. Zhao, S. Zhang, *J. Phys. Chem. B* 118C (2014) 8824.
- [20] T. Leshuk, R. Parviz, P. Everett, H. Krishnakumar, R.A. Varin, F. Gu, *ACS Appl. Mater. Interfaces* 5 (2013) 1892.
- [21] J.-Y. Shin, J.H. Joo, D. Samuelis, J. Maier, *Chem. Mater.* 24 (2012) 543.
- [22] D.C. Cronemeyer, *Phys. Rev.* 113 (1959) 1222.
- [23] D. Jiang, W. Wang, S. Sun, L. Zhang, Y. Zheng, *ACS Catal.* 5 (2015) 613.
- [24] D. Jiang, W. Wang, L. Zhang, Y. Zheng, Z. Wang, *ACS Catal.* 5 (2015) 4851.
- [25] A. Janotti, J. Varley, P. Rinke, N. Umezawa, G. Kresse, C. Van de Walle, *Phys. Rev. B* 81 (2010) 085212.
- [26] S. Wendt, P.T. Sprunger, E. Lira, G.K.H. Madsen, Z. Li, J.Ø. Hansen, J. Matthiesen, A. Blekinge-Rasmussen, E. Lægsgaard, B. Hammer, F. Besenbacher, *Science* 320 (2008) 1755.
- [27] T. Vinodkumar, D.D. Naga, S. Maloth, B.M. Reddy, *J. Chem. Sci.* 127 (2015) 1145.
- [28] Y. Lv, W. Yao, X. Ma, C. Pan, R. Zong, Y. Zhu, *Catal. Sci. Technol.* 3 (2013) 3136.
- [29] M. Kong, Y. Li, X. Chen, T. Tian, P. Fang, F. Zheng, X. Zhao, *J. Am. Chem. Soc.* 133 (2011) 16414.
- [30] L. Liu, Q. Liu, Y. Zheng, Z. Wang, C. Pan, W. Xiao, *J. Phys. Chem. C* 118 (2014) 3471.
- [31] Q. Guo, C. Zhou, Z. Ma, Z. Ren, H. Fan, X. Yang, *Chem. Soc. Rev.* 45 (2016), <http://dx.doi.org/10.1039/C5CS00448A>.
- [32] N.J. Lawrence, J.R. Brewer, L. Wang, T.-S. Wu, J. Wells-Kingsbury, M.M. Ihrig, G. Wang, Y.-L. Soo, W.-N. Mei, C.L. Cheung, *Nano Lett.* 11 (2011) 2666.
- [33] H.F. Wang, R. Kavanagh, Y.L. Guo, Y. Guo, G.Z. Lu, P. Hu, *Angew. Chem. Int. Ed.* 51 (2012) 6657.
- [34] D. Jiang, W. Wang, L. Zhang, R. Qiu, S. Sun, Y. Zheng, *Appl. Catal. B* 165 (2015) 399.
- [35] X. Du, X. Gao, Y. Fu, F. Gao, Z. Luo, K. Cen, J. Colloid Interface Sci. 368 (2012) 406.
- [36] A. Primo, T. Marino, A. Corma, R. Molinari, H. Garcia, *J. Am. Chem. Soc.* 133 (2011) 6930.
- [37] A. Tanaka, K. Hashimoto, H. Kominami, *J. Am. Chem. Soc.* 134 (2012) 14526.
- [38] D. Jiang, W. Wang, E. Gao, L. Zhang, S. Sun, *J. Phys. Chem. C* 117 (2013) 24242.
- [39] Q. Yuan, H.H. Duan, L.L. Li, Z.X. Li, W.T. Duan, L.S. Zhang, W.G. Song, C.H. Yan, *Adv. Mater.* 22 (2010) 1475.
- [40] F. Esch, S. Fabris, L. Zhou, T. Montini, C. Africh, P. Fornasiero, G. Comelli, R. Rosei, *Science* 309 (2005) 752.
- [41] Q. Fu, H. Saltsburg, M. Flytzani-Stephanopoulos, *Science* 301 (2003) 935.
- [42] T. Sakthivel, D. Reid, U. Bhatta, G. Mobus, D. Sayle, S. Seal, *Nanoscale* 7 (2015) 5169.
- [43] T. Naganuma, E. Traversa, *Nanoscale* 6 (2014) 6637.
- [44] J.P. Holgado, G. Munuera, J.P. Espinós, A.R. González-Elipe, *Appl. Surf. Sci.* 158 (2000) 164.
- [45] T. Naganuma, E. Traversa, *Nanoscale* 4 (2012) 4950.
- [46] L.R. Shah, B. Ali, H. Zhu, W. Wang, Y. Song, H. Zhang, S. Shah, J.Q. Xiao, *J. Phys. Chem. C* 113 (2009) 486004.
- [47] M.M. Khan, S.A. Ansari, D. Pradhan, D.H. Han, J. Lee, M.H. Cho, *Ind. Eng. Chem. Res.* 53 (2014) 9754.
- [48] G. Zhu, T. Lin, X. Lu, W. Zhao, C. Yang, Z. Wang, H. Yin, Z. Liu, F. Huang, J. Lin, J. Mater. Chem. A 1 (2013) 9650.
- [49] Z.-Y. Pu, J.-Q. Lu, M.-F. Luo, Y.-L. Xie, *J. Phys. Chem. C* 111 (2007) 18695.
- [50] M. Zhao, M. Shen, J. Wang, *J. Catal.* 248 (2007) 258.
- [51] L. Li, F. Chen, J.-Q. Lu, M.-F. Luo, *J. Phys. Chem. A* 115 (2011) 7972.
- [52] M. Cargnello, J.J.D. Jaén, J.C.H. Garrido, K. Bakhmutsky, T. Montini, J.J.C. Gámez, R.J. Gorte, P. Fornasiero, *Science* 337 (2012) 713.
- [53] D. Wang, X. Pan, G. Wang, Z. Yi, *RSC Adv.* 5 (2015) 22038.
- [54] P. Gélin, M. Promet, *Appl. Catal. B* 39 (2002) 1.
- [55] Y. Lykhach, V. Johánek, H.A. Aleksandrov, S.M. Kozlov, M. Happel, T. Skála, P.S. Petkov, N. Tsud, G.N. Vayssilov, K.C. Prince, K.M. Neyman, V. Matolín, J. Libuda, *J. Phys. Chem. C* 116 (2012) 12103.
- [56] M.K. Nowotny, L.R. Sheppard, T. Bak, J. Nowotny, *J. Phys. Chem. C* 112 (2008) 5275.
- [57] O. Bikondoa, C.L. Pang, R. Ithnin, C.A. Muryn, H. Onishi, G. Thornton, *Nat. Mater.* 5 (2006) 189.
- [58] G. Munuera, V. Rives-Arnau, A. Saucedo, *J. Chem. Soc. Faraday Trans. 75* (1979) 736.
- [59] L. Palmisano, M. Schiavella, A. Sclafani, G. Martra, E. Borello, S. Coluccia, *Appl. Catal. B* 3 (1994) 117.
- [60] H.A. Al-Abadleh, V.H. Grassian, *Langmuir* 19 (2003) 341.
- [61] Z. Wu, M. Li, D.R. Mullins, S.H. Overbury, *ACS Catal.* 2 (2012) 2224.
- [62] A.K.P. Mann, Z. Wu, F.C. Calaza, S.H. Overbury, *ACS Catal.* 4 (2014) 2437.
- [63] Z. Wu, M. Li, S.H. Overbury, *J. Catal.* 285 (2012) 61.
- [64] K.C. Hass, W.F. Schneider, A. Curioni, W. Andreoni, *J. Phys. Chem. B* 104 (2000) 5527.
- [65] Y.-X. Pan, C.-J. Liu, D. Mei, Q. Ge, *Langmuir* 26 (2010) 5551.
- [66] Z.-Z. Yang, L.-N. He, Y.-N. Zhao, B. Li, B. Yu, *Energy Environ. Sci.* 4 (2011) 3971.
- [67] Y.-X. Pan, P. Kuai, Y. Liu, Q. Ge, C.-J. Liu, *Energy Environ. Sci.* 3 (2010) 1322.
- [68] S.H. Szczepankiewicz, A. Colussi, M.R. Hoffmann, *J. Phys. Chem. B* 104 (2000) 9842.